

# Azimuth Resampling Processing for Highly Squinted Synthetic Aperture Radar Imaging With Several Modes

Mengdao Xing, *Member, IEEE*, Yufeng Wu, Yimin D. Zhang, *Senior Member, IEEE*,  
Guang-Cai Sun, *Member, IEEE*, and Zheng Bao, *Life Senior Member, IEEE*

**Abstract**—The linear range walk yields a significant range–azimuth coupling effect in a highly squinted synthetic aperture radar (SAR). Although the linear range walk correction (LRWC) technique can effectively mitigate such coupling effect, it causes azimuth variation in the resulting signal and, as such, the so-called “azimuth-shift invariance” property becomes invalid. In order to eliminate the azimuth variation, a new spectrum processing approach based on azimuth resampling is proposed in this paper. After performing the LRWC, the azimuth resampling is carried out in the 2-D frequency domain and transforms the signal spectrum to be equivalent to that of a broadside SAR. For squinted beam-steering SAR (BS-SAR), e.g., spotlight SAR, sliding spotlight SAR, and Terrain Observation by Progressive Scans SAR, the azimuth resampling is combined with the azimuth signal reconstruction algorithm. As a result, both the azimuth variation, which is induced by the LRWC, and the aliasing, which is caused by antenna beam steering, can be avoided. Therefore, after the azimuth resampling, the squinted SAR data can be focused by exploiting a conventional broadside SAR imaging algorithm. An analysis of the motion error for airborne SAR data processing is also provided. Simulation and real data results show the effectiveness of the proposed algorithm.

**Index Terms**—Azimuth resampling, linear range walk correction (LRWC), squinted beam-steering SAR (BS-SAR), squinted SAR.

## I. INTRODUCTION

SYNTHETIC aperture radar (SAR) is a powerful and well-established microwave remote sensing technique that enables high-resolution measurements of the Earth’s surface. SAR has a good resolution in both range and azimuth directions. The range and azimuth resolutions are determined by the bandwidth of the transmitted signal and the width of the azimuth synthetic aperture, respectively. In addition, SAR is a powerful and effective tool for the retrieval of geographical information because of its capability to work under all weather conditions, day and night [1]–[3]. In a SAR configuration, the angle between

the pointing direction of the antenna beam and the direction perpendicular to the flight path is defined as the squint angle [4]. Specifically, a SAR is referred to as a broadside SAR when the squint angle equals to zero, whereas a squinted SAR implies that the squint angle is negligible.

A number of approaches have been developed to focus the broadside SAR data, such as the range Doppler algorithm (RDA) [5], the chirp scaling algorithm (CSA) [6], the frequency scaling algorithm (FSA) [7], and their extended forms [8]–[10]. For a squinted SAR, on the other hand, data focusing is much more complicated and challenging because of the range–azimuth coupling effect introduced due to the squint angle [11]. As such, traditional imaging algorithms work properly only when the squint angle is negligible. For example, to achieve a 5-m-range resolution, the squint angle should be smaller than about  $5^\circ$  for the CSA and about  $10^\circ$  for the extended CSA (ECSA). As the squint angle and the range resolution increase, the range–azimuth coupling effect becomes negligible, and the space variance of the second range compression (SRC) and the cubic range frequency phase terms becomes more pronounced. The CSA and ECSA do not work properly in this case because they ignore the Doppler and range dependence in the SRC term. By introducing a perturbation function, which is multiplied to the range data either in the time domain [12] or in the frequency domain [13], the nonlinear CSA (NCSA) eliminates the variation of SRC. Thus, the NCSA can be used to handle a higher value of squint angle. Nevertheless, the range dependence of the cubic- and higher order terms remain neglected in the NCSA. Sun *et al.* [14] extended the NCSA by taking higher order terms, e.g., the fourth-order term, into account based on the method of series reversion. However, for highly squinted and high-resolution SAR data processing, a large number of terms should be considered and, as such, the algorithm becomes very complicated. In this case, the range migration algorithm (RMA, or omega-k algorithm) [15]–[17] is a commonly used approach to process highly squinted SAR imageries. The RMA employs the so-called Stolt interpolation for range cell migration (RCM) correction and does not involve approximation.

All the aforementioned algorithms, however, directly deal with the original squinted data and focus on the analysis of the characteristics of the squinted data spectrum. As a result, the 2-D skew spectrum requires a high pulse-repetition frequency (PRF) or an extra computational load in the imaging process

Manuscript received April 27, 2013; revised July 25, 2013 and August 21, 2013; accepted September 8, 2013. This work was supported in part by the National Natural Science Foundation of China under Grants 61222108 and 61301292.

M. Xing, Y. Wu, G.-C. Sun, and Z. Bao are with the National Key Laboratory of Radar Signal Processing, Xidian University, Xi’an 710071, China (e-mail: rsandsgc@126.com; gcsun@xidian.edu.cn).

Y. D. Zhang is with the Center for Advanced Communications, Villanova University, Villanova, PA 19085 USA.

Color versions of one or more of the figures in this paper are available online at <http://ieeexplore.ieee.org>.

Digital Object Identifier 10.1109/TGRS.2013.2281454

due to the increased number of azimuthal samples [11], which are associated with the squint angle and the signal bandwidth.

Another method is to carry out the linear range walk correction (LRWC) first and then to focus the data [18], [19]. Although LRWC can significantly decrease the coupling effect, the signal becomes azimuth dependent and the ‘‘azimuth-shift invariance’’ property no longer holds because, after LRWC is applied, the quadratic RCM (QRCM) and azimuth frequency modulation (FM) rates of targets confined in a range gate will differ to each other. The squinted RDA [18] ignores the azimuth variation and, therefore, can only process low-resolution data observed in a small scene. Based on the principle of nonlinear CS (NCS), Wong and Yeo proposed an azimuth NCS (ANCS) method to eliminate the variation of azimuth FM rates [19]. After LRWC and range compression, a nonlinear chirp perturbation function is applied to each range gate to equalize the FM rates of all targets. Thus, the same azimuth matched filter can be implemented in each range gate. In recent years, further developments of the ANCS algorithm [20]–[22] have been studied to process SAR data for more complicated imaging geometries.

Although the ANCS algorithm can effectively eliminate the variation of azimuth FM rate, it ignores the azimuth variation of QRCM. For highly squinted high-resolution SAR, therefore, the focused results of the range marginal points may suffer from a significant degradation. Zhang *et al.* considered the azimuth-dependent component of QRCM and proposed a method to apply the NCS algorithm to the azimuth data in the range frequency domain before the QRCM correction is applied [23]. However, the processing is complicated.

In order to eliminate the azimuth variation in both QRCM and azimuth FM rate, a new spectrum processing approach based on azimuth resampling is proposed in this paper. In the proposed method, after performing LRWC, the azimuth resampling is carried out through interpolation in the 2-D frequency domain and, as such, converts the signal spectrum to be equivalent to that of a broadside SAR. On the other hand, for beam-steering SAR (BS-SAR), e.g., spotlight SAR, sliding spotlight SAR, and Terrain Observation by Progressive Scans (TOPS) SAR, the azimuth bandwidth is usually much larger than the system’s PRF due to the beam steering. Thus, the azimuth signal becomes aliased in the Doppler domain. To solve this problem, the proposed azimuth resampling is combined with the azimuth signal reconstruction algorithm. As a result, the azimuth variation, which is induced by LRWC, and the aliasing, which is caused by the antenna beam steering, can be both effectively eliminated. After the proposed azimuth resampling is applied, therefore, the squinted SAR data can be focused by exploiting conventional broadside SAR imaging algorithms.

While both the processed algorithm and the RMA exploit interpolation operation, the proposed algorithm has clear advantages over the RMA. First, the required PRF for the proposed algorithm is lower than that for the RMA since the RMA directly deals with the squinted data spectrum whereas the proposed algorithm deals with the signal spectrum after LRWC. As such, the RMA requires a higher number of azimuthal samples than the proposed algorithm, and so is the

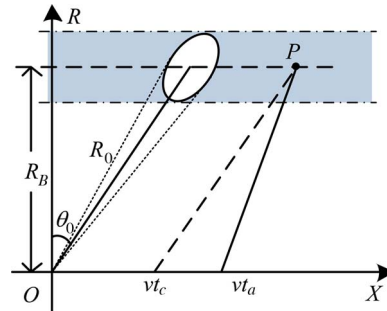


Fig. 1. Squinted SAR imaging geometry.

complexity of the interpolation operations needed in the data processing. Second, the motion compensation (MoCo) of the proposed algorithm is simpler compared with the RMA because the azimuth resampling only affects the residual phase error whereas the Stolt mapping used in the RMA not only affects the residual phase error but also amplifies the residual RCM error [24]. There are some other differences between these two algorithms, such as the processed spectra, the interpolation direction, and the reference frame of the output SAR image.

This paper is organized as follows: Section II reviews the signal model of a squinted SAR and the problem induced by LRWC. Section III introduces the principle of equivalent array and then implements it in the squinted SAR data processing through azimuth resampling. In Section IV, the azimuth resampling and the azimuth signal reconstruction algorithms are combined to process the squinted BS-SAR data. Section V provides an analysis of the impacts of the motion error on the proposed algorithms, particularly on the azimuth resampling operation. Section VI presents the simulations and real data results. Finally, Section VII concludes the paper.

## II. SQUINTED SAR SIGNAL MODEL AND LRWC

### A. Squinted SAR Signal Model

Fig. 1 shows the imaging geometry of a squinted stripmap SAR. In this figure, the SAR sensor travels along the  $x$ -axis, and the velocity is  $v$ .  $\theta_0$  is the center squint angle, and  $R_B$  is the closest range from a point target  $P$  to the trajectory. With reference to the imaging geometry, the slant range distance between the radar and the point target  $P$  is

$$R(t_a) = \sqrt{(R_0 \cos \theta_0)^2 + (R_0 \sin \theta_0 - v(t_a - t_c))^2} \quad (1)$$

where  $R_0$  is the slant range at the center of the aperture,  $t_a$  is the azimuth slow time, and  $t_c$  is the center illuminated time of point  $P$ . For further analysis, (1) is expanded using Taylor’s series

$$R(t_a) = R_0 - v \sin \theta_0 (t_a - t_c) + \frac{v^2 \cos^2 \theta_0}{2R_0} (t_a - t_c)^2 + \frac{v^3 \sin \theta_0 \cos^2 \theta_0}{2R_0^2} (t_a - t_c)^3 + \dots \quad (2)$$

Equation (2) shows that the RCM consists of range walk (i.e., linear term of slow time), range curvature (i.e., quadratic term of slow time), and higher order terms.

Assume that a linear FM signal is transmitted by the radar. Then, the demodulated echoes can be expressed as

$$ss(t, t_a) = w_r \left( t - \frac{2R(t_a)}{c} \right) w_a(t_a - t_c) \times \exp \left( j\pi\gamma \left( t - \frac{2R(t_a)}{c} \right)^2 \right) \exp \left( -j\frac{4\pi}{\lambda} R(t_a) \right) \quad (3)$$

where  $t$  is the fast time,  $c$  is the propagation velocity of light,  $\gamma$  is the FM rate of the transmitted signal, and  $\lambda$  is the wavelength. In addition,  $w_r(\cdot)$  and  $w_a(\cdot)$  denote the envelopment of the transmitted signal and the azimuth window function, respectively.

To derive the 2-D frequency expression, which is crucial for the imaging algorithm design [6], we take the Fourier transform (FT) with respect to the fast time on both sides of (3), yielding

$$SS(f_r, t_a) = W_r(f_r)w_a(t_a - t_c) \exp \left( -j\pi\frac{f_r^2}{\gamma} \right) \times \exp \left( -j\frac{4\pi}{c}(f_c + f_r)R(t_a) \right) \quad (4)$$

where  $f_r$  is the range frequency,  $f_c$  is the carried frequency, and  $W_r(\cdot)$  is the FT of  $w_r(\cdot)$ .

### B. LRWC

Due to the existence of the first-order term of  $t_a$  in (2), i.e., range walk in RCM, the coupling effect between the range and the azimuth in a squinted SAR is more pronounced than that of a broadside SAR. By applying LRWC, which is the delay processing of the received signal, we can substantially mitigate the coupling effect. The corresponding correction function is expressed as

$$H_{LRWC}(f_r, t_a) = \exp \left( -j\frac{4\pi v \sin \theta_0}{c}(f_c + f_r)t_a \right). \quad (5)$$

Multiplying (5) with (4), we obtain

$$SS'(f_r, t_a) = W_r(f_r)w_a(t_a - t_c) \exp \left( -j\pi\frac{f_r^2}{\gamma} \right) \times \exp \left( -j\frac{4\pi}{c}(f_c + f_r)(R(t_a) + v \sin \theta_0 t_a) \right). \quad (6)$$

Using the stationary phase method (SPM) [25], we can obtain the 2-D frequency spectrum of (6), which can be expressed as

$$SS(f_r, f_a) = W_r(f_r)W_a(f_a) \exp \left( -j\pi\frac{f_r^2}{\gamma} \right) \times \exp \left( -j\frac{2\pi}{v}(f_a + f_{dc})(R_0 \sin \theta_0 + vt_c) \right) \times \exp \left( -j4\pi R_0 \cos \theta_0 \sqrt{\left( \frac{f_c + f_r}{c} \right)^2 - \left( \frac{f_a + f_{dc}}{2v} \right)^2} \right) \quad (7)$$

where  $f_a$  is the azimuth frequency,  $f_{dc} = (2v \sin \theta_0/c)(f_c + f_r)$ , and  $W_a(\cdot)$  is the FT of  $w_a(\cdot)$ . In order to analyze the

migration character of the signal, let

$$\sqrt{\left( \frac{f_c + f_r}{c} \right)^2 - \left( \frac{f_a + f_{dc}}{2v} \right)^2} \approx A + Bf_r \quad (8)$$

where

$$\begin{cases} A = \sqrt{\left( \frac{f_c}{c} \right)^2 - \left( \frac{f_a}{2v} + \frac{\sin \theta_0}{c} f_c \right)^2} \\ B = \frac{\frac{f_c}{c} - \left( \frac{f_a}{2v} + \frac{\sin \theta_0}{c} f_c \right) \sin \theta_0}{c \sqrt{\left( \frac{f_c}{c} \right)^2 - \left( \frac{f_a}{2v} + \frac{\sin \theta_0}{c} f_c \right)^2}} \end{cases} \quad (8a)$$

Substituting (8) into (7), the 2-D frequency spectrum can be rewritten as

$$SS(f_r, f_a) = W_r(f_r)W_a(f_a) \exp \left( -j\pi\frac{f_r^2}{\gamma} \right) \exp(-j4\pi R_0 \cos \theta_0 A) \times \exp \left( -j2\pi \left( f_a + \frac{2v \sin \theta_0}{\lambda} \right) \frac{(R_0 \sin \theta_0 + vt_c)}{v} \right) \times \exp \left( -j4\pi \left( R_0 \cos \theta_0 \frac{\frac{f_c}{c} - \left( \frac{f_a}{2v} + \frac{\sin \theta_0}{c} f_c \right) \sin \theta_0}{\sqrt{\left( \frac{f_c}{c} \right)^2 - \left( \frac{f_a}{2v} + \frac{\sin \theta_0}{c} f_c \right)^2}} + \sin \theta_0 (R_0 \sin \theta_0 + vt_c) \right) \frac{f_r}{c} \right). \quad (9)$$

From (9), the migration curve can be expressed as

$$R(f_a) = R_0 \cos \theta_0 \frac{\frac{f_c}{c} - \left( \frac{f_a}{2v} + \frac{\sin \theta_0}{c} f_c \right) \sin \theta_0}{\sqrt{\left( \frac{f_c}{c} \right)^2 - \left( \frac{f_a}{2v} + \frac{\sin \theta_0}{c} f_c \right)^2}} + \sin \theta_0 (R_0 \sin \theta_0 + vt_c) \approx (R_0 + vt_c \sin \theta_0) + \frac{R_0}{4v^2} \left( \frac{c}{f_c} \right)^2 \frac{1}{\cos^2 \theta_0} f_a^2. \quad (10)$$

In the second row of (10), the first term determines the target's position after range compression, whereas the second term is the QRCM term that needs to be corrected before azimuth focusing. After performing QRCM correction and range compression, therefore, the target will appear at

$$R(f_a = 0) = R_0 + vt_c \sin \theta_0 = R_0 + X_c \sin \theta_0 = r_s \quad (11)$$

where  $X_c = vt_c$ . Equation (11) indicates that, after LRWC, the point targets whose azimuth position do not equal to zero will have added shifting along the range direction, i.e., targets located in the same range cell will have different distances. Since both the QRCM and the azimuth FM rate are related to the target distance, this means that, after LRWC, the QRCM and azimuth FM rates of targets confined in a range gate will differ from each other. Fig. 2 illustrates the QRCM after LRWC. The dashed curves represent the respective target positions before LRWC, whereas the solid curves show the positions after LRWC. In Fig. 2, points with different QRCMs, such as points A, C, and E, are located in the same range cell after LRWC.

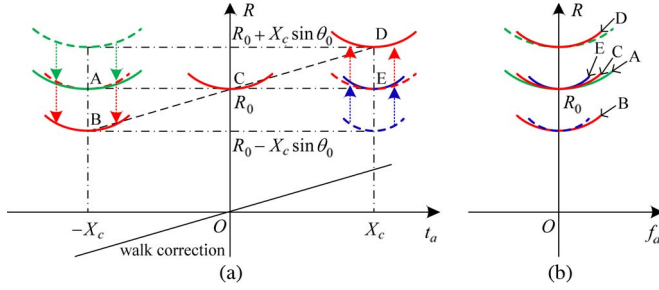


Fig. 2. QRCMs after LRWC in (a) the azimuth time domain and (b) the azimuth frequency domain.

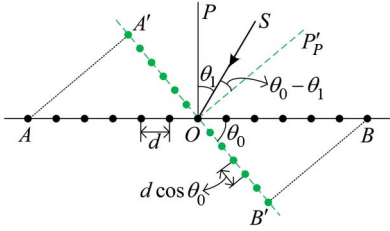


Fig. 3. Illustration of an equivalent array.

Therefore, after LRWC, the ‘‘azimuth-shift invariance’’ property no longer applies. In order to solve this problem, the principle of equivalent array is proposed and used to process the squinted SAR data in the next section.

### III. EQUIVALENT ARRAY PRINCIPLE AND ITS APPLICATION IN SAR

As previously discussed, although LRWC can effectively reduce the range–azimuth coupling effect, it yields the signal to be azimuth variant and thus causes new problems to the data focusing. In order to eliminate the azimuth variation, the principle of equivalent array is introduced and used to process the squinted SAR data in this section.

#### A. Principle of Equivalent Array

In an equivalent array depicted in Fig. 3,  $AB$  denotes a linear array, and the distance between two adjacent array elements is  $d$ .  $OP$  is perpendicular to  $AB$ .  $A'B'$  denotes the equivalent array of  $AB$  with a projection angle of  $\theta_0$ , and  $OP'$  is perpendicular to  $A'B'$ . As such, the distance between two adjacent array elements in  $A'B'$  is  $d \cos \theta_0$ .

Assume that there is a single frequency signal with an incident angle of  $\theta_1$  and the wavelength is  $\lambda$ . The echo signal

received by the  $n$ th element at arrays  $AB$  and  $A'B'$  can be respectively written as

$$\begin{cases} s_{AB}(t, n) = s(t) \exp(j\varphi_0 + j\frac{4\pi}{\lambda}nd \sin \theta_1) \\ s_{A'B'}(t, n) = s(t) \exp(j\varphi_0 + j\frac{4\pi}{\lambda}nd \cos \theta_0 \sin(\theta_1 - \theta_0)) \end{cases} \quad (12)$$

where  $s(t)$  and  $\varphi_0$  are the amplitude and phase of the received signal at reference point  $O$ , respectively, and  $n = -((N - 1)/2), \dots, -1, 0, 1, \dots, ((N - 1)/2)$ , where  $N$  is the number of elements. Essentially, LRWC is the delay processing of the received signal such that the beam is directed to the center squint angle. Therefore, after LRWC is applied, the signal received at the  $n$ th element of array  $AB$  becomes

$$\begin{aligned} s_{AB-LRWC}(t, n) \\ = s(t) \exp\left(j\varphi_0 + j\frac{4\pi}{\lambda}nd \sin \theta_1 - j\frac{4\pi}{\lambda}nd \sin \theta_0\right). \end{aligned} \quad (13)$$

Assume that the angular separation between  $\theta_1$  and  $\theta_0$  is small, the following approximation can be used:

$$\sin \theta_1 - \sin \theta_0 \approx \sin(\theta_1 - \theta_0) \cos \theta_0. \quad (14)$$

Then, the signal in (13) can be approximated as

$$s_{AB-appr}(t, n) \approx s(t) \exp\left(j\varphi_0 + j\frac{4\pi}{\lambda}nd \cos \theta_0 \sin(\theta_1 - \theta_0)\right). \quad (15)$$

It is evident from (15) that, after applying LRWC and the approximation, the echo signal received at array  $AB$  becomes equivalent to the signal received at array  $A'B'$ , as depicted in the second expression of (12). The approximation of (14), however, is accurate only for a small array. For a large array, such as a synthetic array that typically has a large synthetic aperture, the approximation will result in an negligible error, which can be described as

$$\Delta\varphi = \frac{4\pi}{\lambda}nd(\sin \theta_1 - \sin \theta_0 - \sin(\theta_1 - \theta_0) \cos \theta_0). \quad (16)$$

In SAR, particularly for a high squint angle and a high resolution, the error will result in the deprivation of the focused imaging and thus needs to be taken into account. By taking the FT with respect to  $n$ , we obtain (17) shown at the bottom of the page. On the other hand, the Doppler frequency can be expressed as

$$\begin{cases} f_{a-AB-LRWC} = \frac{v}{\lambda}(\sin \theta_1 - \sin \theta_0) = \frac{d\text{PRF}}{\lambda}(\sin \theta_1 - \sin \theta_0) \\ f_{a-A'B'} = \frac{v}{\lambda} \sin(\theta_1 - \theta_0) = \frac{d \cos \theta_0 \text{PRF}}{\lambda} \sin(\theta_1 - \theta_0). \end{cases} \quad (18)$$

$$\begin{cases} S_{AB-LRWC}(t, k) = s(t) \exp(j\varphi_0) \sum_{n=1}^N \exp(j\varphi_0 + j\frac{4\pi}{\lambda}nd(\sin \theta_1 - \sin \theta_0)) \exp(-j2\pi \frac{n}{N}k) \\ \quad = s(t) \exp(j\varphi_0) \delta\left(k - \frac{2dN(\sin \theta_1 - \sin \theta_0)}{\lambda}\right) \\ S_{A'B'}(t, k) = s(t) \exp(j\varphi_0) \sum_{n=1}^N \exp(j\frac{4\pi}{\lambda}nd \cos \theta_0 \sin(\theta_1 - \theta_0)) \exp(-j2\pi \frac{n}{N}k) \\ \quad = s(t) \exp(j\varphi_0) \delta\left(k - \frac{2Nd \cos \theta_0 \sin(\theta_1 - \theta_0)}{\lambda}\right). \end{cases} \quad (17)$$

Substituting (18) into (17), we have

$$\begin{cases} S_{AB-LRWC}(t, k) = s(t) \exp(j\varphi_0) \delta\left(k - 2N \frac{f_{a\_AB-LRWC}}{\text{PRF}}\right) \\ S_{A'B'}(t, k) = s(t) \exp(j\varphi_0) \delta\left(k - 2N \frac{f_{a\_A'B'}}{\text{PRF}}\right). \end{cases} \quad (19)$$

It is observed in (19) that the only difference between these two expressions is between  $f_{a\_AB-LRWC}$  and  $f_{a\_A'B'}$ . Thus, if we can eliminate this difference, then the data received at array  $AB$  will become completely equivalent to the signal received at array  $A'B'$ . Toward this end, note in (18) that the difference of the two expressions is between  $(\sin \theta_1 - \sin \theta_0)$  and  $\cos \theta_0 \sin(\theta_1 - \theta_0)$ . This difference can be eliminated by letting

$$\begin{aligned} f'_{a\_AB-LRWC} &= \frac{f_{a\_AB-LRWC}}{\sin \theta_1 - \sin \theta_0} \cos \theta_0 \sin(\theta_1 - \theta_0) \\ &= \frac{d \text{PRF}}{\lambda} \cos \theta_0 \sin(\theta_1 - \theta_0). \end{aligned} \quad (20)$$

In addition, from the first expression of (18), we have  $\sin \theta_1 = (\lambda f_{a\_AB-LRWC}/v) + \sin \theta_0$ . Therefore

$$\begin{aligned} \sin(\theta_1 - \theta_0) &= \sin \theta_1 \cos \theta_0 - \cos \theta_1 \sin \theta_0 \\ &= \cos \theta_0 \left( \frac{\lambda f_{a\_AB-LRWC}}{v} + \sin \theta_0 \right) \\ &\quad - \sin \theta_0 \sqrt{1 - \left( \frac{\lambda f_{a\_AB-LRWC}}{v} + \sin \theta_0 \right)^2}. \end{aligned} \quad (21)$$

Substituting (21) into (20), we can get

$$\begin{aligned} f'_{a\_AB-LRWC} &= \frac{d \text{PRF}}{\lambda} \\ &\quad \times \cos \theta_0 \left( \cos \theta_0 \left( \frac{\lambda f_{a\_AB-LRWC}}{v} + \sin \theta_0 \right) \right. \\ &\quad \left. - \sin \theta_0 \sqrt{1 - \left( \frac{\lambda f_{a\_AB-LRWC}}{v} + \sin \theta_0 \right)^2} \right) \end{aligned} \quad (22)$$

i.e.,

$$\begin{aligned} \frac{f'_{a\_AB-LRWC}}{\cos \theta_0} &= \cos \theta_0 \left( f_{a\_AB-LRWC} + \frac{v}{\lambda} \sin \theta_0 \right) \\ &\quad - \sin \theta_0 \sqrt{\left( \frac{v}{\lambda} \right)^2 - \left( f_{a\_AB-LRWC} + \frac{v}{\lambda} \sin \theta_0 \right)^2}. \end{aligned} \quad (23)$$

Then, the difference between the two signals can be eliminated.

### B. Application of Equivalent Array Principle in SAR

Because the azimuth variation in a squinted configuration is due to the LRWC, it vanishes if the difference between the

data of the squinted configuration after LRWC and that of the broadside configuration is eliminated. Compared with the array signal, SAR merely replaces the space samples by the time samples under the ‘‘go-stop-go’’ assumption. Therefore, (23) can be used to eliminate the difference.

In a SAR system, a wideband signal is usually transmitted. Due to the round-trip delay, (23) needs to be modified as

$$\begin{aligned} \frac{f'_a}{\cos \theta_0} &= \cos \theta_0 \left( f_a + \frac{2v \sin \theta_0}{c} (f_c + f_r) \right) \\ &\quad - \sin \theta_0 \sqrt{\left( \frac{2v}{c} (f_c + f_r) \right)^2 - \left( f_a + \frac{2v \sin \theta_0}{c} (f_c + f_r) \right)^2} \\ &= \cos \theta_0 (f_a + f_{dc}) \\ &\quad - \sin \theta_0 \sqrt{\left( \frac{2v}{c} (f_c + f_r) \right)^2 - (f_a + f_{dc})^2}. \end{aligned} \quad (24)$$

In order to eliminate the azimuth variance induced by the LRWC, the 2-D frequency spectrum in (7) is divided into two parts: the azimuth-invariance part and the azimuth-variance part. This can be realized by substituting (11) into (7). After some straightforward steps, we obtain

$$\begin{aligned} SS(f_r, f_a) &= W_r(f_r) W_a(f_a) \exp\left(-j\pi \frac{f_r^2}{\gamma}\right) \\ &\quad \times \exp\left(-j2\pi \frac{2r_s}{c} \left( \frac{c}{2v} (f_a + f_{dc}) \sin \theta_0 \right. \right. \\ &\quad \left. \left. + \cos \theta_0 \sqrt{(f_c + f_r)^2 - \left( \frac{c}{2v} (f_a + f_{dc}) \right)^2} \right)\right) \\ &\quad \times \exp\left(-j2\pi \frac{X_c \cos \theta_0}{v} \left( (f_a + f_{dc}) \cos \theta_0 \right. \right. \\ &\quad \left. \left. - \sin \theta_0 \sqrt{\left( \frac{2v}{c} (f_c + f_r) \right)^2 - (f_a + f_{dc})^2} \right)\right). \end{aligned} \quad (25)$$

Further substituting (24) into (25) yields the following 2-D frequency spectrum:

$$\begin{aligned} SS(f_r, f'_a) &= W_r(f_r) W_a(f'_a) \exp\left(-j\pi \frac{f_r^2}{\gamma}\right) \exp\left(-j2\pi \frac{X_c}{v} f'_a\right) \\ &\quad \times \exp\left(-j4\pi r_s \sqrt{\left( \frac{f_c + f_r}{c} \right)^2 - \left( \frac{f'_a}{2v \cos \theta_0} \right)^2}\right). \end{aligned} \quad (26)$$

Compared with the spectrum of a broadside SAR [4], one can find that the two spectra are identical, except that the effective velocity is  $v \cos \theta_0$  instead of  $v$  in the squinted SAR imaging mode. Therefore, after the azimuth resampling, we

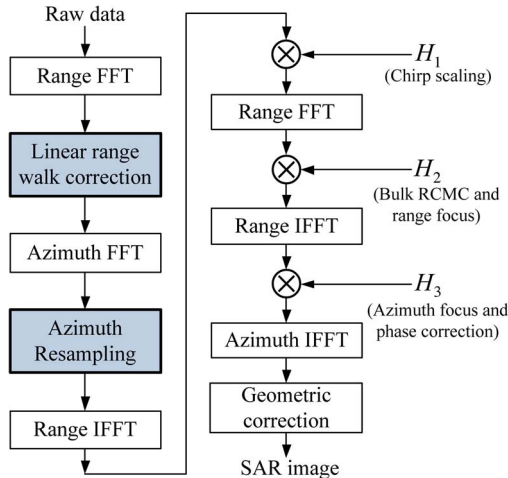


Fig. 4. Flowchart of the azimuth-resampling-based CS algorithm.

can complete the data focusing by the traditional broadside SAR imaging algorithms, such as RDA, CSA, and ECSA. In particular, the flowchart of the overall processing is depicted in Fig. 4, when the CSA is used to focus the data. The functions  $H_1$ ,  $H_2$ , and  $H_3$  are the standard phase functions used in the CSA and can be found in [6]. Because the variable substitution in (24) can be implemented by azimuth resampling of the signal spectrum, the approach proposed in this paper can be referred to as the azimuth-resampling-based algorithm.

It is clear from (26) that the target located at  $(R_0, X_c)$  is focused at  $(r_s, X_c)$  by the proposed algorithm. This means that there is a geometric distortion in the focused SAR image and, hence, a geometric correction should be implemented in the  $(f_r, t_a)$  domain after azimuth compression.

#### IV. EXTENSION TO SQUINTED BS-SAR

For applications with different requirements, many imaging modes have been developed in the literature, such as spotlight SAR [3], sliding spotlight SAR [26], and TOPS SAR [27]. For these SAR modes, the antenna is steered to compress or extend the synthetic time and, thus, to reduce or improve the spatial resolutions. Since all the three SAR modes require beam steering, a uniform name, i.e., BS-SAR, is used in this paper for convenience. The stripmap mode can be considered as a special case of BS-SAR, in which the velocity of beam steering equals to zero. The BS-SAR involves either a broadside imaging geometry or a squinted imaging geometry, as illustrated in Fig. 5.

Due to the beam steering of BS-SAR during the data acquisition interval, the azimuth bandwidth of the bulk data may be much greater than the PRF. In this case, the azimuth signal is aliased in the Doppler domain. To overcome this problem, some methods based on subapertures are proposed [7], [28], [29]. The data received at the entire synthetic aperture are divided into multiple subapertures so that the azimuth bandwidth in each subaperture is smaller than the PRF. Utilizing this characteristics, one can correct the RCM using a traditional stripmap algorithm in each subaperture and then combine the subaperture data and focus the azimuth data by azimuth

matched filtering (AMF) [28], spectral analysis (SPECAN) [4], or baseband azimuth scaling [29]. However, it needs azimuth block division and subaperture recombination to avoid signal spectrum blurring. The PRF, instantaneous bandwidth, and FM rate all affect subaperture division directly. If a low PRF is used, i.e., it is only slightly larger than the instantaneous bandwidth, the data must be divided into a large number of blocks. On the other hand, a high PRF results in increased data redundancy.

In order to avoid the complicated subaperture processing, full-aperture imaging algorithms have also been proposed for BS-SAR [26], [30]–[32]. In these methods, the first step is to reconstruct the original signal spectrum. This can be realized by convoluting the azimuth signal with a reference function and then compensating the function in the azimuth frequency domain. The flowchart is shown in Fig. 6(a), and the functions described therein are given as [31]

$$S_{\text{ref}}(t_a) = \exp\left(j\pi \frac{2v^2 t_a^2}{\lambda R_{\text{ref}}}\right) \quad (27)$$

$$S_{\text{ref}}(t_{a1}) = \exp\left(j\pi \frac{2v^2 t_{a1}^2}{\lambda R_{\text{ref}}}\right) \quad (28)$$

$$S_{\text{com}}(f_{a1}) = \exp\left(j\pi \frac{\lambda R_{\text{ref}}}{2v^2} f_{a1}^2\right) \quad (29)$$

where  $R_{\text{ref}}$  is the closest distance from the rotation center to the radar trajectory. After obtaining the signal spectrum without aliasing, the traditional stripmap algorithm can be used to complete the range compression and RCM correction. Finally, AMF or SPECAN can be used to focus the azimuth data. However, for BS-SAR, it is difficult to obtain a spectrum that is unaliased in both the azimuth frequency domain and the azimuth time domain without data extension (i.e., zero padding). Although the azimuth convolution operation can retrieve the unaliased spectrum, the signal is aliased in the azimuth time domain [31], [32].

All these algorithms focus on the broadside BS-SAR configuration. For the squinted BS-SAR case, the signal has serious range–azimuth coupling effect and blurred spectrum. As such, the data focusing is much more complicated than the broadside BS-SAR. An extended two-step algorithm is proposed in [33] for squinted spotlight SAR data processing. In this algorithm, the LRWC is first performed to reduce the range–azimuth coupling effect and then to focus the data. However, the method ignores the azimuth variation yielded by the LRWC. For a large scene, it requires the full scene to be divided into a large number of subscenes in the azimuth direction and then refocuses the data in each subscene. Finally, all the subimages are merged together to obtain a well-focused full-scene image. However, high-resolution images may suffer from degraded image resolution due to some approximations, which are in the derivation of the algorithm. Furthermore, large-scene high-resolution data may result in a prohibitively high number of subscenes. For squinted sliding spotlight SAR and squinted TOPS SAR, to our knowledge, no efficient algorithm is available.

In Section III, we proposed a new spectrum processing approach based on azimuth resampling. After LRWC and azimuth

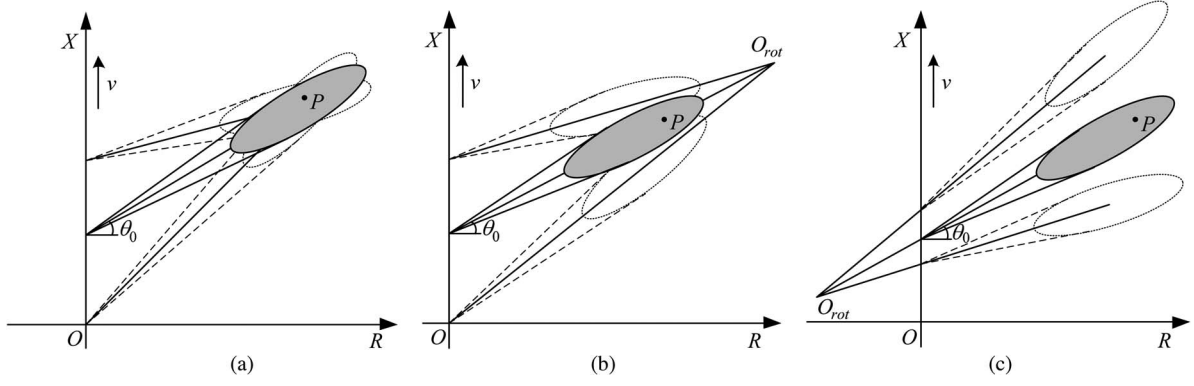


Fig. 5. Imaging geometry of a squinted BS-SAR. (a) Squinted spotlight SAR. (b) Squinted sliding spotlight SAR. (c) Squinted TOPS SAR.

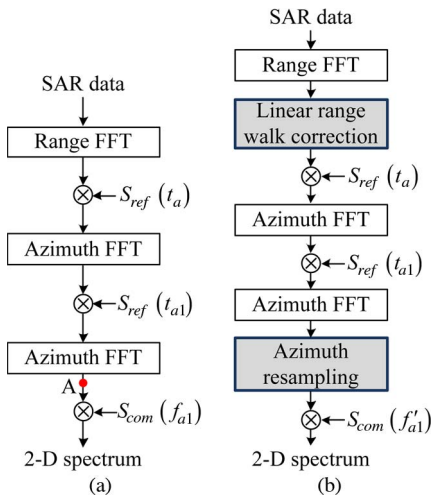


Fig. 6. Flowchart of BS-SAR signal spectrum reconstruction. (a) Broadside BS-SAR. (b) Squinted BS-SAR.

resampling, the squinted SAR signal spectrum becomes equivalent to the spectrum of a broadside SAR. Therefore, the data can be focused by a conventional broadside SAR imaging algorithm. If the same approach can be applied to BS-SAR such that the squinted BS-SAR signal spectrum becomes equivalent to that of broadside BS-SAR, the data focusing of the BS-SAR would be significantly simplified as well. In this part, we will combine the azimuth resampling with the azimuth signal reconstruction algorithm, and the flowchart is depicted in Fig. 6(b). The reference functions in Fig. 6(b) are the same as those in Fig. 6(a), except that the effective velocity becomes  $v \cos \theta_0$  instead of  $v$ . Comparing Fig. 6(a) and (b), it is clear that only two added operations, i.e., LRWC and azimuth resampling, are required to obtain the signal spectrum for the squinted BS-SAR.

It is noted in Fig. 6(b) that the azimuth resampling is performed before multiplying with the compensated function rather than resampling the signal spectrum directly. The reason is that, while the spectrum obtained through convolution is not blurred in the azimuth frequency domain, it is aliased in the azimuth time domain and, therefore, we cannot resample a signal that is blurred. By analyzing the time–frequency distribution of the signal in each step of the signal reconstruction algorithm, we find that the signal after the second azimuth FT but before

compensating the signal  $S_{com}(f_{a1})$  [i.e., the signal at point A in Fig. 6(a)] is not aliased in both the azimuth frequency domain and the azimuth time domain. Therefore, we can resample the signal at point A and the compensated signal  $S_{com}(f_{a1})$  and then obtain their product. As such, the azimuth variation caused by LRWC can be eliminated. After performing the processing, as depicted in Fig. 6(b), the spectrum of the squinted BS-SAR will be equivalent to that of a broadside BS-SAR and, therefore, the data can be focused by using one of the existing broadside BS-SAR imaging algorithms.

## V. MOTION ERROR ANALYSIS

For airborne SAR, an aircraft is often sensitive to atmospheric turbulence and, as such, it may suffer from serious trajectory deviations. In this case, MoCo is an essential procedure to obtain a well-focused image. Here, we analyze the impacts of the motion error on the proposed algorithms, particularly on the azimuth resampling operation. According to [12], the MoCo can be divided into two steps: the first step consists of phase and envelope corrections with respect to the reference range and height, whereas the second step accommodates the range variant aberrations. Since the first-order MoCo can be carried out by utilizing inertial navigation system and inertial measurement unit (INS/IMU) measurements, here we only consider the residual motion error.

After coarse MoCo, the slant range, described in (1), is modified as

$$\hat{R}(t_a) = R(t_a) + \Delta R(t_a) \quad (30)$$

where  $\Delta R(t_a)$  denotes the residual motion error. As such, the signal after LRWC becomes

$$\begin{aligned} Ss(f_r, t_a) &= \exp\left(-j\pi \frac{f_r^2}{\gamma}\right) \\ &\times \exp\left(-j \frac{4\pi}{c} (f_c + f_r) (R(t_a) + v \sin \theta_0 t_a)\right) \\ &\times \exp\left(-j \frac{4\pi}{c} (f_c + f_r) \Delta R(t_a)\right). \end{aligned} \quad (31)$$

In (31), only the exponential terms of the received signal is considered. Applying the azimuth FT to (31) yields

$$\begin{aligned} SS(f_r, f_a) &= \int Ss'(f_r, t_a) \exp(-j2\pi f_a t_a) dt_a \\ &= \int \exp\left(-j\pi \frac{f_r^2}{\gamma}\right) \\ &\quad \times \exp\left(-j\frac{4\pi}{c}(f_c + f_r)(R(t_a) + v \sin \theta_0 t_a)\right) \\ &\quad \times \exp\left(-j\frac{4\pi}{c}(f_c + f_r)\Delta R(t_a)\right) \\ &\quad \times \exp(-j2\pi f_a t_a) dt_a. \end{aligned} \quad (32)$$

According to the SPM, the first derivative of the phase function with respect to  $t_a$  in (32) is set to zero, i.e.,

$$\begin{aligned} -\frac{4\pi}{c}(f_c + f_r) \frac{\partial (R(t_a) + v \sin \theta_0 t_a)}{\partial t_a} \\ -\frac{4\pi}{c}(f_c + f_r) \frac{\partial \Delta R(t_a)}{\partial t_a} - 2\pi f_a = 0. \end{aligned} \quad (33)$$

Due to the lack of information about the range error, it is impossible to solve the equation precisely. However, according to [24], the residual phase error is nominal compared with the phase history of the point target reference and, thus, can be ignored. Then, the approximate stationary phase point can be derived as

$$t_a^* = \frac{R_0 \sin \theta_0}{v} - \frac{R_0 \cos \theta_0 (f_{dc} + f_a)}{2v^2 \sqrt{\left(\frac{f_c + f_r}{c}\right)^2 - \left(\frac{f_{dc} + f_a}{2v}\right)^2}} + t_c. \quad (34)$$

By Substituting (34) into (32), the spectrum becomes

$$\begin{aligned} SS(f_r, f_a) &= \exp\left(-j\pi \frac{f_r^2}{\gamma}\right) \exp\left(-j\frac{2\pi}{v}(f_{dc} + f_a)(R_0 \sin \theta_0 + vt_c)\right) \\ &\quad \times \exp\left(-j4\pi R_0 \cos \theta_0 \sqrt{\left(\frac{f_c + f_r}{c}\right)^2 - \left(\frac{f_{dc} + f_a}{2v}\right)^2}\right) \\ &\quad \times \exp\left(-j\frac{4\pi}{c}(f_c + f_r)\Delta R(t_a^*)\right). \end{aligned} \quad (35)$$

Substituting  $R_0 = r_s - X_c \sin \theta_0$  into (35) results in (36), shown at the bottom of the page. Then, by applying the azimuth resampling and substituting (24) into (36), we obtain

$$\begin{aligned} SS(f_r, f'_a) &= \exp\left(-j2\pi \frac{X_c}{v} f'_a\right) \\ &\quad \times \exp\left(-j4\pi r_s \sqrt{\left(\frac{f_c + f_r}{c}\right)^2 - \left(\frac{f'_a}{2v \cos \theta_0}\right)^2}\right) \\ &\quad \times \exp\left(-j\pi \frac{f_r^2}{\gamma}\right) \exp\left(-j\frac{4\pi}{c}(f_c + f_r)\Delta R(t_x)\right) \end{aligned} \quad (37)$$

where

$$\begin{aligned} t_x &= \frac{R_0 \sin \theta_0}{v} \\ &\quad - \frac{2R_0 \left( f'_a + \sin \theta_0 \sqrt{\left(\frac{2v}{c}(f_c + f_r)\right)^2 - \left(\frac{f'_a}{\cos \theta_0}\right)^2} \right)}{\sqrt{\left(\frac{2v}{c}(f_c + f_r)\right)^2 - \left(\frac{f'_a}{\cos \theta_0}\right)^2} - \frac{\sin \theta_0}{\cos^2 \theta_0} f'_a} + t_c. \end{aligned} \quad (37a)$$

After that, the RCM correction and range compression is carried out and the resulting signal can be expressed as

$$\begin{aligned} SS(f_r, f'_a) &= \exp\left(-j2\pi \frac{X_c}{v} f'_a\right) \\ &\quad \times \exp\left(-j2\pi \frac{r_s}{v \cos \theta_0} \sqrt{\left(\frac{2v \cos \theta_0}{\lambda}\right)^2 - (f'_a)^2}\right) \\ &\quad \times \exp\left(-j2\pi \frac{2r_s}{c} f_r\right) \exp\left(-j\frac{4\pi}{c}(f_c + f_r)\Delta R(t_x)\right). \end{aligned} \quad (38)$$

By taking the inverse FT (IFT) with respect to the azimuth frequency on both sides of (38), we obtain

$$\begin{aligned} Ss(f_r, t'_a) &= \int \exp\left(-j2\pi \frac{X_c}{v} f'_a\right) \exp\left(-j2\pi \frac{2r_s}{c} f_r\right) \end{aligned}$$

---


$$\begin{aligned} SS(f_r, f_a) &= \exp\left(-j\pi \frac{f_r^2}{\gamma}\right) \exp\left(-j\frac{4\pi}{c}(f_c + f_r)\Delta R(t_a^*)\right) \\ &\quad \times \exp\left(-j2\pi \frac{2r_s}{c} \left(\frac{c}{2v}(f_{dc} + f_a) \sin \theta_0 + \cos \theta_0 \sqrt{(f_c + f_r)^2 - \left(\frac{c}{2v}(f_{dc} + f_a)\right)^2}\right)\right) \\ &\quad \times \exp\left(-j2\pi \frac{X_c \cos \theta_0}{v} \left((f_{dc} + f_a) \cos \theta_0 - \sin \theta_0 \sqrt{\left(\frac{2v}{c}(f_c + f_r)\right)^2 - (f_{dc} + f_a)^2}\right)\right). \end{aligned} \quad (36)$$

$$\begin{aligned} & \times \exp \left( -j2\pi \frac{r_s}{v \cos \theta_0} \sqrt{\left( \frac{2v \cos \theta_0}{\lambda} \right)^2 - (f'_a)^2} \right) \\ & \times \exp \left( -j \frac{4\pi}{c} (f_c + f_r) \Delta R(t_x) \right) \exp(j2\pi f'_a t'_a) df'_a \end{aligned} \quad (39)$$

where  $t'_a$  is the new slow time corresponding to  $f'_a$ . In order to obtain an analytic expression of  $Ss(f_r, t'_a)$ , we use the SPM and have

$$\begin{aligned} -\frac{X_c}{v} - \frac{r_s}{v \cos \theta_0} \frac{\partial}{\partial f'_a} \left( \sqrt{\left( \frac{2v \cos \theta_0}{\lambda} \right)^2 - (f'_a)^2} \right) \\ - \frac{2}{c} (f_c + f_r) \frac{\partial \Delta R(x)}{\partial f'_a} + f'_a = 0. \end{aligned} \quad (40)$$

Due to the small value of the error term, we neglect its contribution into the stationary point calculation and obtain

$$f'_a = \frac{2v^2 \cos^2 \theta_0}{\lambda r_s \sqrt{1 + \left( \frac{v \cos \theta_0}{r_s} \left( \frac{X_c}{v} - t'_a \right) \right)^2}} \left( \frac{X_c}{v} - t'_a \right). \quad (41)$$

Substituting (41) into (39) yields

$$\begin{aligned} Ss(f_r, t'_a) \\ = \exp \left( -j \frac{4\pi}{\lambda} \sqrt{r_s^2 + \left( v \cos \theta_0 \left( \frac{X_c}{v} - t'_a \right) \right)^2} \right) \\ \times \exp \left( -j2\pi \frac{2r_s}{c} f_r \right) \\ \times \exp \left( -j \frac{4\pi}{c} (f_c + f_r) \Delta R \left( \frac{r_s}{r_s + v \sin \theta_0} (t'_a - t_c) \right) \right). \end{aligned} \quad (42)$$

Applying the IFT with respect to  $f_r$ , we obtain the following range-compressed signal:

$$\begin{aligned} ss(t, t'_a) \\ = \text{sinc} \left( B \left( t - \frac{2r_s}{c} - 2\Delta R \left( \frac{r_s}{r_s + v \sin \theta_0} (t'_a - t_c) \right) \right) / c \right) \\ \times \exp \left( -j \frac{4\pi}{\lambda} \sqrt{r_s^2 + \left( v \cos \theta_0 \left( \frac{X_c}{v} - t'_a \right) \right)^2} \right) \\ \times \exp \left( -j \frac{4\pi}{\lambda} \Delta R \left( \frac{r_s}{r_s + v \sin \theta_0} (t'_a - t_c) \right) \right). \end{aligned} \quad (43)$$

Since the residual motion error is small after applying coarse MoCo based on the INS/IMU measurements, the residual RCM error is usually smaller than a quarter of the range sampling cell and, thus, can be ignored. As such, it can be observed from (43) that the azimuth resampling only affects the residual phase error. Therefore, the residual MoCo can be implemented after

TABLE I  
SIMULATION PARAMETERS

|                      |                 |
|----------------------|-----------------|
| Center frequency     | 9.65GHz         |
| Pulse bandwidth      | 300MHz          |
| Antenna length       | 0.8m            |
| Velocity             | 120m/s          |
| Center line distance | 10km            |
| Squint angle         | 45°             |
| Point A              | (-1000,-1000) m |
| Point B              | (0,0) m         |
| Point C              | (1000,1000) m   |

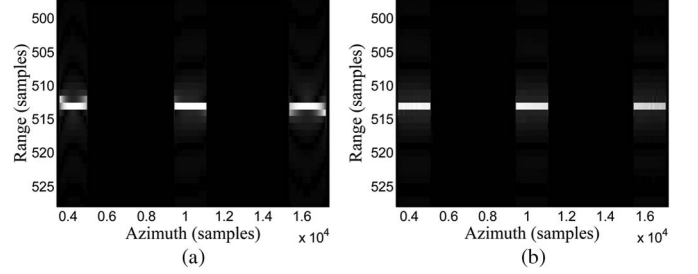


Fig. 7. Range compression results via the CSA. (a) Without azimuth resampling. (b) With azimuth resampling.



Fig. 8. Simulation results via the CSA. (a) Without azimuth resampling. (b) With azimuth resampling.

RCM correction and range compression by using the method described in [34].

## VI. SIMULATION RESULTS AND REAL DATA EXAMPLES

To validate the effectiveness of the proposed approach, simulation results and real data examples are presented in this section.

### A. Results From Simulated Data

*Simulation Results I:* The objective of this simulation is to validate the effectiveness of azimuth resampling in eliminating the azimuth variation of QRCM and azimuth FM rate. The SAR system works in the squinted stripmap mode, and the main simulation parameters and point coordinates are shown in Table I.

Fig. 7 shows the QRCM correction and range compression results via the CSA. In particular, Fig. 7(a) and (b) respectively shows the results without and with the application of the azimuth resampling. It is evident that the residual QRCM of all the point targets, which is observed in Fig. 7(a), is well compensated after the azimuth resampling is applied, as clearly depicted in Fig. 7(b).

By performing AMF, the three targets are focused, as shown in Fig. 8. Hereinto, Fig. 8(a) is the imaging result without applying azimuth resampling. Although the target in the scene center is well focused, the targets on the edges remain highly

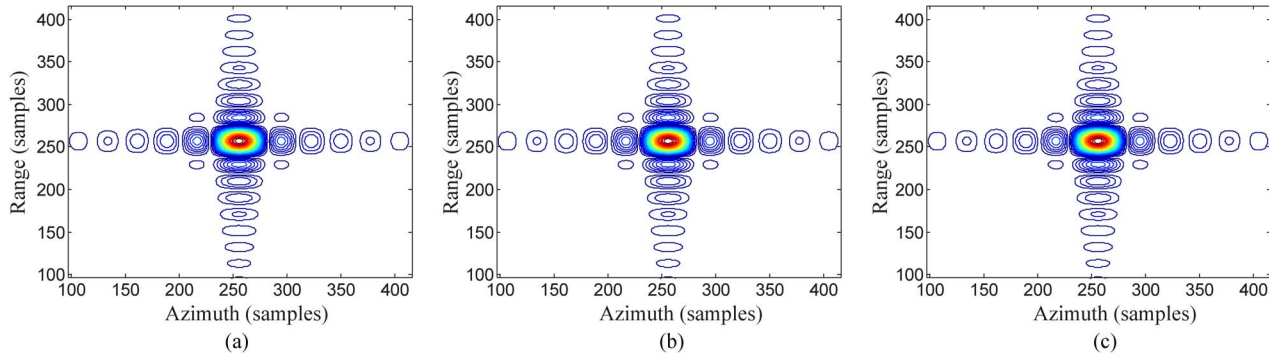


Fig. 9. Contour plots of the impulse response function for the three point targets using the proposed approach.

TABLE II  
PARAMETERS OF THE FOCUSED TARGETS

| Point target | Range     |           |                | Azimuth   |           |                |
|--------------|-----------|-----------|----------------|-----------|-----------|----------------|
|              | PSLR (dB) | ISLR (dB) | Resolution (m) | PSLR (dB) | ISLR (dB) | Resolution (m) |
| A            | -13.27    | -9.80     | 0.5137         | -13.38    | -10.01    | 0.4083         |
| B            | -13.27    | -9.80     | 0.5137         | -13.26    | -9.91     | 0.4078         |
| C            | -13.27    | -9.80     | 0.5137         | -13.34    | -9.96     | 0.4083         |

TABLE III  
COMMON PARAMETERS

|                      |           |
|----------------------|-----------|
| Center frequency     | 9.65GHz   |
| Pulse duration       | 2 $\mu$ s |
| PRF                  | 360Hz     |
| Antenna length       | 0.8m      |
| Velocity             | 120m/s    |
| Center line distance | 20km      |
| Squint angle         | 45°       |

defocused. After the azimuth resampling, on the other hand, all three targets are well focused, as shown in Fig. 8(b), because the space variation of the azimuth FM rate is eliminated.

To study the performance of the imaging results using the proposed approach, Fig. 9 shows the contour plots of the impulse response function for the three point targets. The peak sidelobe ratio (PSLR), the integrated sidelobe ratio (ISLR), and the resolution are also investigated to evaluate the focus quality, and the results are summarized in Table II. In Fig. 9 and Table II, we can further conclude that all three targets are well focused.

*Simulation Results II:* In this part, we present simulation results for three BS-SAR modes. The common parameters shared by the three BS-SAR modes are listed in Table III, whereas the mode-specific parameters are presented in Table IV. A  $9 \times 9$  dot-matrix is arranged in the simulated scene. The geometry of the scene is presented in Fig. 10, and the scene size is changed with the imaging mode.

The simulated TOPS SAR data are used to analyze the characteristics of the signal spectrum before and after the proposed method is applied. Fig. 11(a) shows the signal spectrum of the raw data. It is evident that these data have azimuth aliases in the 2-D frequency domain. It is clear in Fig. 11(b) that such aliasing is eliminated after the proposed method, as described in Fig. 6(b), is applied. In addition, the signal spectrum is

TABLE IV  
MODE-SPECIFIC PARAMETERS

| Modes                               | Squinted Spotlight SAR | Squinted sliding Spotlight SAR | Squinted TOPS SAR    |
|-------------------------------------|------------------------|--------------------------------|----------------------|
| Pulse bandwidth (MHz)               | 1000                   | 500                            | 30                   |
| Sample frequency (MHz)              | 1200                   | 600                            | 40                   |
| Rotation center range (km)          | 20                     | 48.6259                        | -1.7415              |
| Scene size (Range $\times$ Azimuth) | 2.0km $\times$ 0.8km   | 3.0km $\times$ 1.6km           | 6.0km $\times$ 4.8km |

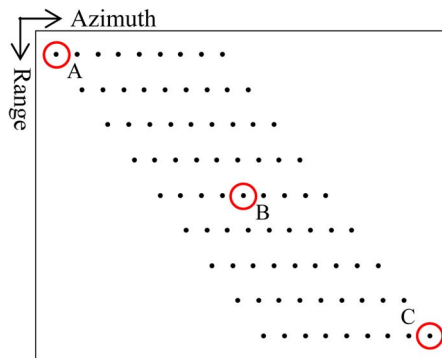


Fig. 10. Geometry of simulated point targets.

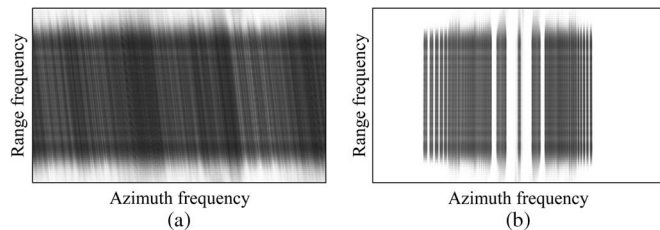


Fig. 11. Signal spectrum of TOPS SAR (a) before and (b) after applying the proposed method.

no longer skew, which is consonant with the spectrum of a broadside SAR.

After obtaining the signal spectrum by using the proposed approach, the spotlight SAR is focused via the method in [30] and the sliding spotlight and TOPS SAR are focused via the method described in [31]. To evaluate the performance of the imaging results, three point targets, which are respectively denoted as A, B, and C, are considered. Fig. 12 shows, from left to right, the contour plots of the impulse response function

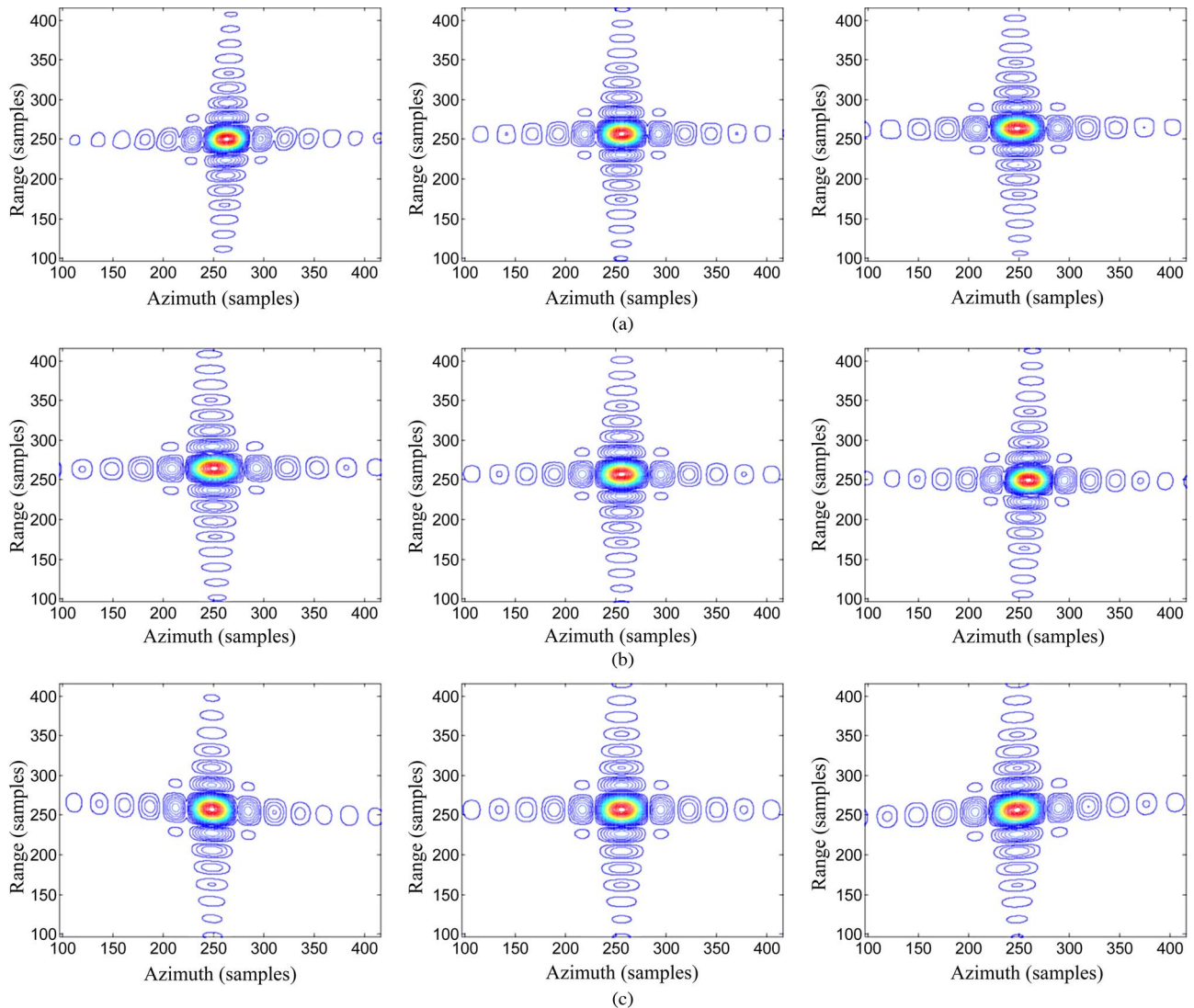


Fig. 12. Simulation results. The subimages, from left to right, in every row correspond to targets A, B, and C, respectively. (a) Squinted spotlight SAR. (b) Squinted sliding spotlight SAR. (c) Squinted TOPS SAR.

for the three point targets, and Table V gives the PSLR, the ISLR, and the resolution. It is clear in Fig. 12 and Table V that the point targets, no matter in the scene center or on the scene edges, are well focused.

### B. Real Data Results

In this subsection, we present real data results. Since squinted spotlight SAR data and squinted sliding spotlight SAR data are not available to us, only the results of the squinted stripmap mode and the squinted TOPS mode are presented.

*Results of Squinted Stripmap SAR:* The real airborne data of an experimental X-band SAR with the squinted stripmap mode is used to verify the performance of the proposed approach. The bandwidth of the transmitted signal is 180 MHz, and the center squint angle is  $50^\circ$ . Since the motion of the airborne SAR was affected by air disturbance, the MoCo is an important step. For these SAR data, the motion error is small, and thus, the MoCo is implemented using the method described in [35]. The

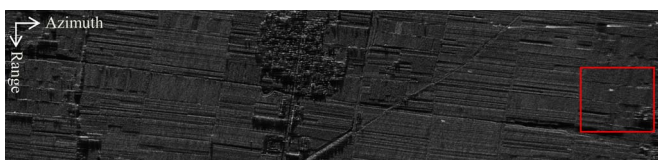
envelopment error is estimated and compensated for the data after LRWC but before range compression, whereas the phase error is estimated and compensated for the data after range compression.

Fig. 13 shows the imaging results using the conventional squinted RDA. Fig. 13(a) shows the result without azimuth resampling. As the azimuth variation exists in the QRCM and azimuth FM rate, the SAR image is defocused in the edge regions. This is evident in Fig. 14(a), which is the local enlargement of Fig. 13(a) for the red rectangular region. Fig. 13(b) is the imaging result with azimuth resampling, and Fig. 14(b) gives its local enlargement for the red rectangular region. Since the space variation along the azimuth is eliminated by azimuth resampling, the entire scene is well focused, including the edge regions.

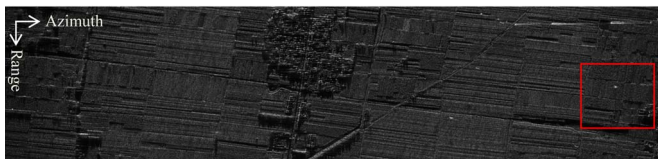
*Result of Squinted TOPS SAR:* The raw airborne data of an experimental Ku-band SAR with the squinted TOPS mode were collected on December 18, 2010. The main parameters of the SAR system are tabulated in Table VI. After obtaining the

TABLE V  
PARAMETERS OF THE FOCUSED TARGETS

|                                |              | Range     |           |                | Azimuth   |           |                |
|--------------------------------|--------------|-----------|-----------|----------------|-----------|-----------|----------------|
| Modes                          | Point target | PSLR (dB) | ISLR (dB) | Resolution (m) | PSLR (dB) | ISLR (dB) | Resolution (m) |
| Squinted spotlight SAR         | A            | -13.04    | -10.08    | 0.1527         | -13.63    | -10.39    | 0.1222         |
|                                | B            | -13.27    | -9.96     | 0.1518         | -13.27    | -10.37    | 0.1311         |
|                                | C            | -13.16    | -9.93     | 0.1533         | -13.07    | -10.09    | 0.1439         |
| Squinted sliding spotlight SAR | A            | -13.17    | -9.94     | 0.3098         | -13.25    | -10.13    | 0.2781         |
|                                | B            | -13.19    | -9.83     | 0.3082         | -13.36    | -10.21    | 0.2569         |
|                                | C            | -13.02    | -9.75     | 0.3069         | -12.97    | -9.92     | 0.2348         |
| Squinted TOPS SAR              | A            | -13.05    | -10.26    | 5.0704         | -13.25    | -10.07    | 3.4223         |
|                                | B            | -13.19    | -9.93     | 5.1379         | -13.26    | -9.82     | 4.6707         |
|                                | C            | -13.10    | -9.97     | 5.1316         | -13.20    | -10.04    | 6.8553         |

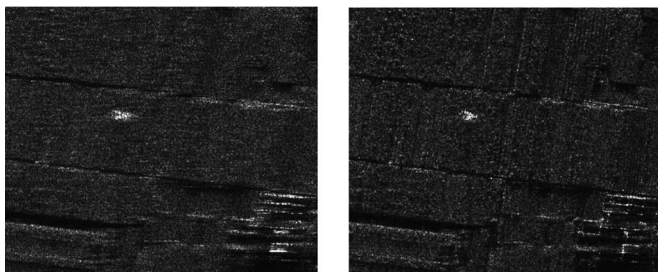


(a)

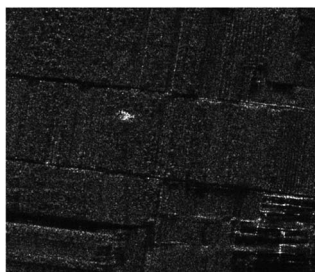


(b)

Fig. 13. Imaging results using the conventional squinted RDA. (a) Without azimuth resampling. (b) With azimuth resampling.



(a)



(b)

Fig. 14. Local enlargement of Fig. 13. (a) Without azimuth resampling. (b) With azimuth resampling.

signal spectrum using the steps depicted in Fig. 6(b), the data are focused, as shown in Fig. 15. It is evident from this figure that the image is well focused.

## VII. CONCLUSION

A squinted SAR suffers from the range–azimuth coupling effect of the raw data over the coherent aperture time. While the LRWC can effectively reduce such coupling effect, it introduces azimuth variation in the signal. In this paper, we have proposed an azimuth-resampling-based approach, which eliminates the

TABLE VI  
MAIN SYSTEM PARAMETERS

|                       |             |
|-----------------------|-------------|
| Wave band             | Ku-band     |
| Pulse bandwidth       | 100MHz      |
| PRF                   | 1000Hz      |
| Squint angle          | 46.1°       |
| Steering angle        | 34.5°~57.6° |
| Center line of scene  | 10.2km      |
| Rotation center range | -306m       |

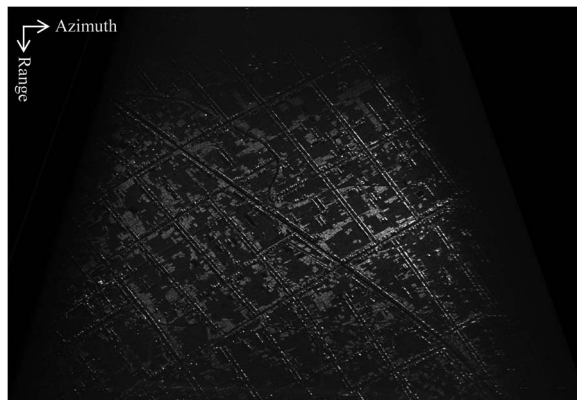


Fig. 15. Result from the airborne squinted TOPS SAR data.

azimuth variation and transforms the spectrum of a squinted SAR to be equivalent to that of a broadside SAR. As such, the resulting data can be focused by using one of the existing broadside SAR imaging algorithms. In addition, for a squinted BS-SAR, the azimuth resampling is combined with the azimuth signal reconstruction algorithm to avoid subaperture or sub-scene processing. The effectiveness of the proposed method has been verified using both simulated and real data results.

## ACKNOWLEDGMENT

The authors would like to thank the anonymous reviewers for their helpful and constructive comments and suggestions, which have helped to greatly improve the presentation of this paper.

## REFERENCES

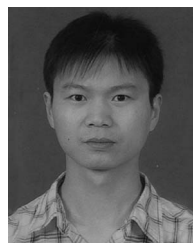
- [1] J. C. Curlander and R. N. McDonough, *Synthetic Aperture Radar: System and Signal Processing*. New York, NY, USA: Wiley, 1991.
- [2] M. Soumekh, *Synthetic Aperture Radar Signal Processing with MATLAB Algorithms*. New York, NY, USA: Wiley, 1999.
- [3] W. G. Carrara, R. S. Goodman, and R. M. Majewski, *Spotlight Synthetic Aperture Radar—Signal Processing and Algorithms*. Boston, MA, USA: Artech House, 1995.
- [4] I. G. Cumming and F. H. Wong, *Digital Processing of Synthetic Aperture Radar Data: Algorithms and Implementation*. Norwood, MA, USA: Artech House, 2005.
- [5] M. Y. Jin and C. Wu, "A SAR correlation algorithm which accommodates large range migration," *IEEE Trans. Geosci. Remote Sens.*, vol. GRS-22, no. 6, pp. 592–597, Nov. 1984.
- [6] R. K. Raney, H. Runge, R. Bamler, I. G. Cumming, and F. H. Wong, "Precision SAR processing using chirp scaling," *IEEE Trans. Geosci. Remote Sens.*, vol. 32, no. 4, pp. 786–799, Jul. 1994.
- [7] J. Mittermayer, A. Moreira, and O. Loffeld, "Spotlight SAR data processing using the frequency scaling algorithm," *IEEE Trans. Geosci. Remote Sens.*, vol. 37, no. 5, pp. 2198–2214, Sep. 1999.
- [8] A. M. Smith, "A new approach to range-Doppler SAR processing," *Int. J. Remote Sens.*, vol. 12, no. 2, pp. 235–251, Feb. 1991.
- [9] A. Moreira, J. Mittermayer, and R. Scheiber, "Extended chirp scaling algorithm for air- and spaceborne SAR data processing in stripmap and ScanSAR imaging modes," *IEEE Trans. Geosci. Remote Sens.*, vol. 34, no. 5, pp. 1123–1136, Sep. 1996.
- [10] D. Y. Zhu, M. W. Shen, and Z. D. Zhu, "Some aspects of improving the frequency scaling algorithm for dechirped SAR data processing," *IEEE Trans. Geosci. Remote Sens.*, vol. 46, no. 6, pp. 1579–1588, Jun. 2008.
- [11] G. W. Davidson and I. G. Cumming, "Signal properties of spaceborne squint-mode SAR," *IEEE Trans. Geosci. Remote Sens.*, vol. 35, no. 3, pp. 611–617, May 1997.
- [12] A. Moreira and Y. Huang, "Airborne SAR processing of highly squinted data using a chirp scaling approach with integrated motion compensation," *IEEE Trans. Geosci. Remote Sens.*, vol. 32, no. 5, pp. 1029–1040, Sep. 1994.
- [13] G. W. Davidson, I. G. Cumming, and M. R. Ito, "A chirp scaling approach for processing squint mode SAR data," *IEEE Trans. Aerosp. Electron. Syst.*, vol. 32, no. 1, pp. 121–133, Jan. 1996.
- [14] G. C. Sun, M. D. Xing, Y. Liu, L. Sun, Z. Bao, and Y. R. Wu, "Extended NCS based on method of series reversion for imaging of highly squinted SAR," *IEEE Geosci. Remote Sens. Lett.*, vol. 8, no. 3, pp. 446–450, May 2011.
- [15] C. Cafforio, C. Prati, and F. Rocca, "SAR data focusing using seismic migration techniques," *IEEE Trans. Aerosp. Electron. Syst.*, vol. 27, no. 2, pp. 194–207, Mar. 1991.
- [16] G. Fornaro, E. Sansosti, R. Lanari, and M. Tesauro, "Role of processing geometry in SAR raw data focusing," *IEEE Trans. Aerosp. Electron. Syst.*, vol. 38, no. 2, pp. 441–454, Apr. 2002.
- [17] A. Reigber, E. Alivizatos, A. Potsis, and A. Moreira, "Extended wavenumber-domain synthetic aperture radar focusing with integrated motion compensation," *Proc. Inst. Elect. Eng.—Radar Sonar Navig.*, vol. 153, no. 3, pp. 301–310, Jun. 2006.
- [18] F. H. Wong and I. G. Cumming, "Error sensitivities of a secondary range compression algorithm for processing squinted satellite SAR data," in *Proc. IGARSS*, Vancouver, BC, Canada, 1989, pp. 2584–2587.
- [19] F. H. Wong and T. S. Yeo, "New applications of nonlinear chirp scaling in SAR data processing," *IEEE Trans. Geosci. Remote Sens.*, vol. 39, no. 5, pp. 946–953, May 2001.
- [20] X. L. Qiu, D. H. Hu, and C. B. Ding, "An improved NLCS algorithm with capability analysis for one-stationary BiSAR," *IEEE Trans. Geosci. Remote Sens.*, vol. 46, no. 10, pp. 3179–3186, Oct. 2008.
- [21] G. C. Sun, X. W. Jiang, M. D. Xing, Z. J. Qiao, Y. R. Wu, and Z. Bao, "Focus improvement of highly squinted data based on azimuth nonlinear scaling," *IEEE Trans. Geosci. Remote Sens.*, vol. 49, no. 6, pp. 2308–2322, Jun. 2011.
- [22] D. X. An, X. T. Huang, T. Jin, and Z. M. Zhou, "Extended nonlinear chirp scaling algorithm for high-resolution highly squint SAR data focusing," *IEEE Trans. Geosci. Remote Sens.*, vol. 50, no. 9, pp. 3595–3609, Sep. 2012.
- [23] S. X. Zhang, M. D. Xing, X. G. Xia, L. Zhang, R. Guo, and Z. Bao, "Focus improvement of high-squint SAR based on azimuth dependence of quadratic range cell migration correction," *IEEE Geosci. Remote Sens. Lett.*, vol. 10, no. 1, pp. 150–154, Jan. 2013.
- [24] L. Zhang, J. L. Sheng, M. D. Xing, Z. J. Qiao, T. Xiong, and Z. Bao, "Wavenumber-domain autofocusing for highly squinted UAV SAR imagery," *IEEE Sensors J.*, vol. 12, no. 5, pp. 1574–1588, May 2012.
- [25] E. L. Key, E. N. Fowle, and R. D. Haggarty, "A method of designing signals of large time-bandwidth product," *IRE Intern. Conv. Rec.*, vol. 4, pp. 146–154, Mar. 1961.
- [26] R. Lanari, S. Zoffoli, E. Sansosti, G. Fornaro, and F. Serafino, "New approach for hybrid strip-map/spotlight SAR data focusing," *Proc. Inst. Elect. Eng.—Radar, Sonar Navig.*, vol. 148, no. 6, pp. 363–372, Dec. 2001.
- [27] F. D. Zan and A. M. Guarnieri, "TOPS: Terrain observation by progressive scan," *IEEE Trans. Geosci. Remote Sens.*, vol. 44, no. 9, pp. 2352–2360, Sep. 2006.
- [28] J. Mittermayer and A. Moreira, "Spotlight SAR processing using the extended chirp scaling algorithm," in *Proc. IEEE IGARSS*, Singapore, Aug. 1997, pp. 2021–2023.
- [29] P. Prats, R. Scheiber, J. Mittermayer, A. Meta, and A. Moreira, "Processing of sliding spotlight and TOPS SAR data using baseband azimuth scaling," *IEEE Trans. Geosci. Remote Sens.*, vol. 48, no. 2, pp. 770–780, Feb. 2010.
- [30] R. Lanari, M. Tesauro, E. Sansosti, and G. Fornaro, "Spotlight SAR data focusing based on a two-step processing approach," *IEEE Trans. Geosci. Remote Sens.*, vol. 39, no. 9, pp. 1993–2004, Sep. 2001.
- [31] G. C. Sun, M. D. Xing, Y. Wang, Y. F. Wu, Y. R. Wu, and Z. Bao, "Sliding spotlight and TOPS SAR data processing without subaperture," *IEEE Geosci. Remote Sens. Lett.*, vol. 8, no. 6, pp. 1036–1040, Nov. 2011.
- [32] G. Engen and Y. Larsen, "Efficient full aperture processing of TOPS mode data using the moving band chirp Z-transform," *IEEE Trans. Geosci. Remote Sens.*, vol. 49, no. 10, pp. 3688–3693, Oct. 2011.
- [33] D. X. An, X. T. Huang, T. Jin, and Z. M. Zhou, "Extended two-step focusing approach for squinted spotlight SAR imaging," *IEEE Trans. Geosci. Remote Sens.*, vol. 50, no. 7, pp. 2889–2900, Jul. 2012.
- [34] L. Zhang, Z. J. Qiao, M. D. Xing, L. Yang, and Z. Bao, "A robust motion compensation approach for UAV SAR imagery," *IEEE Trans. Geosci. Remote Sens.*, vol. 50, no. 8, pp. 3202–3218, Aug. 2012.
- [35] F. Zhou, Q. Wan, M. Xing, and Z. Bao, "A novel method of motion compensation for airborne high squint synthetic aperture radar," *Acta Electron. Sin.*, vol. 35, no. 3, pp. 463–468, Mar. 2007.



**Mengdao Xing** (M'04) was born in Zhejiang, China, in November 1975. He received the B.S. and Ph.D. degrees in electrical engineering from Xidian University, Xi'an, China, in 1997 and 2002, respectively.

He is currently a Full Professor with the National Key Laboratory of Radar Signal Processing, Xidian University. He is also with the National Key Laboratory of Microwave Imaging Technology, Institute of Electronics, Chinese Academy of Sciences, Beijing, China. He has authored or coauthored two books and published over 200 papers. His research interests

include synthetic aperture radar (SAR), inversed SAR, and sparse signal processing.



**Yufeng Wu** was born in Zhejiang, China, in 1985. He received the Master's degree in electrical engineering in 2009 from Xidian University, Xi'an, China, where he is currently working toward the Ph.D. degree at the National Key Laboratory of Radar Signal Processing.

His research interests include multichannel SAR imaging and Doppler parameter estimation.



**Yimin D. Zhang** (SM'01) received the Ph.D. degree from the University of Tsukuba, Tsukuba, Japan, in 1988.

He joined the faculty of the Department of Radio Engineering, Southeast University, Nanjing, China, in 1988. From 1995 to 1997, he was a Technical Manager with the Communication Laboratory Japan, Kawasaki, Japan, and from 1997 to 1998, he was a Visiting Researcher with ATR Adaptive Communications Research Laboratories, Kyoto, Japan. Since 1998, he has been with Villanova University,

Villanova, PA, USA, where he is currently a Research Professor with the Center for Advanced Communications and the Director of the Wireless Communications and Positioning Laboratory. He has more than 200 publications in the area of statistical signal and array processing for communications and radar applications, including wireless networks, cooperative communications, MIMO systems, source localization and target tracking, synthetic aperture radar, over-the-horizon radar, passive sensing, jammer suppression, time-frequency analysis, radio-frequency identification, and image processing.

Dr. Zhang is an Associate Editor of the *Journal of the Franklin Institute* and an Editor of the *Signal Processing* journal. He is an Associate Editor of the IEEE TRANSACTIONS ON SIGNAL PROCESSING and was an Associate Editor of the IEEE SIGNAL PROCESSING LETTERS from 2006 to 2010.



**Zheng Bao** (M'80–SM'90–LSM'09) was born in Jiangsu, China. He received the B.Eng. degree from the Communication Engineering Institution of China, Xi'an, China, in 1953.

He is currently a Professor with Xidian University, Xi'an, China, where he is also the Chairman of the academic board of the National Key Laboratory of Radar Signal Processing. He has authored or coauthored six books and published over 300 papers. His current research fields include space-time adaptive processing, radar imaging (SAR/ISAR), automatic

target recognition, and over-the-horizon-radar signal processing.



**Guang-Cai Sun** (M'13) was born in Hubei, China, in December 1984. He received the Master's degree in communications engineering from the Post and Telecommunication Institution, Xi'an, China, in 2006 and the Ph.D. degree in electrical engineering from Xidian University, Xi'an, China, in 2012.

He is currently a Researcher with the National Key Laboratory of Radar Signal Processing, Xidian University. He has authored or coauthored one book and published over 40 papers. His research interests include imaging of several SAR modes, moving target

detection, and imaging.